

A deep learning approach to the measurement of long-lived memory kernels from Generalised Langevin Dynamics

Max Kerr Winter, Ilian Pihlajamaa, Vincent E. Debets, and Liesbeth M. C. Janssen

Department of Applied Physics, Eindhoven University of Technology, P.O. Box 513, 5600 MB Eindhoven, The Netherlands

(Dated: February 28, 2023)

Memory effects are ubiquitous in a wide variety of complex physical phenomena, ranging from glassy dynamics and metamaterials to climate models. The Generalised Langevin Equation (GLE) provides a rigorous way to describe memory effects via the so-called memory kernel in an integro-differential equation. However, the memory kernel is often unknown, and accurately predicting or measuring it via e.g. a numerical inverse Laplace transform remains a herculean task. Here we describe a novel method using deep neural networks (DNNs) to measure memory kernels from dynamical data. As proof-of-principle, we focus on the notoriously long-lived memory effects of glassy systems, which have proved a major challenge to existing methods. Specifically, we learn a training set generated with the Mode-Coupling Theory (MCT) of hard spheres. Our DNNs are remarkably robust against noise, in contrast to conventional techniques which require ensemble averaging over many independent trajectories. Finally, we demonstrate that a network trained on data generated from analytic theory (hard-sphere MCT) generalises well to data from simulations of a different system (Brownian Weeks-Chandler-Andersen particles). We provide a general pipeline, KernelLearner, for training networks to extract memory kernels from any non-Markovian system described by a GLE. The success of our DNN method applied to glassy systems suggests deep learning can play an important role in the study of dynamical systems that exhibit memory effects.

I. INTRODUCTION

Non-Markovian systems, i.e. those that exhibit memory effects, pose a number of major challenges to both analytic and computational analysis. This issue is of particular importance as such systems occur across many different areas of modern physics, for example climate models [1], protein interaction networks [2], and the behaviour of supercooled liquids and glasses [3, 4], among many others.

A common, and very general, framework for describing non-Markovian dynamics in continuous time is the Generalised Langevin Equation (GLE), where memory effects are included via a so-called memory kernel. GLEs are a common occurrence across statistical physics as they are produced by the Mori-Zwanzig projection operator formalism [5–7]. This formalism starts with a memoryless (e.g. Hamiltonian) system in a very high dimensional space, and projects the dynamics onto a lower dimensional space consisting of degrees of freedom that are of theoretical interest or are experimentally accessible. The price paid for this dimensionality reduction is the emergence of memory effects in the low dimensional dynamics.

Glasses and supercooled liquids are particularly challenging non-Markovian systems to study as they experience complex dynamics over a wide range of length and time scales, with memory effects lasting multiple orders of magnitude in time. The Mori-Zwanzig method has proved to be very popular in the field of glassy physics, and in particular forms the basis of Mode-Coupling Theory (MCT), a first-principles, self-consistent framework of the glass transition [3, 5, 8–11]. To date, there is no complete theory of the glass transition, and MCT is no exception. Although the Mori-Zwanzig method is exact, it results in an intractable expression for the memory kernel which must then be approximated in a number of ways, varying in complexity depending on the flavour of MCT [9, 12–16]. This fact emphasises the memory kernel as an ob-

ject of particular importance to glassy physics, as it is the point at which an exact theory is abandoned in favour of approximations.

For both glassy and other non-Markovian systems, a GLE of some autocorrelation function, y , can be written in the overdamped limit as

$$y'(t) + \Omega y(t) + \int_{-\infty}^t d\tau K(\tau) y'(t - \tau) = 0, \quad (1)$$

where K is the memory kernel, and Ω , the so-called frequency term, is a parameter that is in general known, which describes the memoryless evolution of y . In general GLEs also contain a random force term, which is removed from Eq. 1 by taking the correlation of a variable with itself to get the autocorrelation y . In MCT, y is the autocorrelation function of density fluctuations. Equations with the form of Eq. 1 are also called memory equations. The question of how to study K given y at first appears simple. By applying a Laplace transform to Eq. 1 the kernel can be disentangled from its convolution with y' , resulting in an explicit expression for K ,

$$K(t) = \mathcal{L}^{-1} \left[\frac{y(0) - (s + \Omega)\mathcal{L}[y]}{s\mathcal{L}[y] - y(0)} \right], \quad (2)$$

where $\mathcal{L}[f(t)](s) = \int_0^\infty e^{-st} f(t) dt$ is the Laplace transform of a function, $f(t)$. The complexity arises from the fact that in practice performing an inverse Laplace transform is a major challenge.

The difficulties of performing a numerical inverse Laplace transform are well known [17, 18], and the extent of this problem is nicely summarised by Epstein and Schotland: “Our results give cogent reasons for the general sense of dread most mathematicians feel about inverting the Laplace transform” [19]. Laplace inversion is an example of an ill-posed inverse problem, where information is lost during any numerical implementation of the forward transform, making the inverse

difficult if not impossible. This effect can be demonstrated by considering the forward Laplace transform of a function expressed as a Fourier series, $\mathcal{L}[f(t)] = \mathcal{L}[\sum_i a_i \sin(\omega_i t) + \sum_j b_j \cos(\omega_j t)]$. The Laplace transforms of \sin and \cos are $\mathcal{L}[\sin(\omega t)](\tau) = \omega/(\omega^2 + \tau^2)$, and $\mathcal{L}[\cos(\omega t)](\tau) = \tau/(\omega^2 + \tau^2)$ respectively. As such, the amplitude of high-frequency components in $f(t)$ are suppressed by the ω^2 in the denominators of the respective Laplace transforms. Above some critical ω^* , the high-frequency components become indistinguishable from noise (either experimental or numerical) and hence are unrecoverable by the inverse transform. Consequently, numerical inverse Laplace transforms are very sensitive to noise, with even numerical round-off errors potentially overwhelming the signal.

Many authors in the soft matter and glassy physics communities have taken an alternative approach to determining the memory kernel, whereby an implicit Volterra integral equation for K is constructed from pair-wise correlation functions [20–23]. Such correlation functions are constructed by taking an ensemble average over a large number of trajectories of particle-based simulations. A variety of different numerical methods have been used to successfully solve such equations for the short time memory effects of various systems [24–27].

An alternative to both explicit Laplace inversion, and solving a Volterra equation, is to use a minimisation approach to approximate the kernel. The problem of performing the inverse Laplace transform in Eq. 2 can be reformulated as finding some \bar{K} such that $|\mathcal{L}[\bar{K}] - \mathcal{L}[K]| < \epsilon$, for some $\epsilon \in \mathbb{R}$ that can be set arbitrarily small [18]. As the high-frequency parts of \bar{K} and K are lost in the forward transform, this minimisation problem does not have a unique solution. Consequently, it is helpful to include a regularisation functional, \mathcal{R} , resulting in the minimisation problem $|\mathcal{L}[\bar{K}] - \mathcal{L}[K]| + |\lambda \mathcal{R}[\bar{K}]| < \epsilon$, where λ is a parameter to control the strength of the regularisation. A simple regularisation technique is to penalise low order derivatives in the solution, i.e. $\mathcal{R}[\bar{K}] = \bar{K}''$, resulting in a smooth \bar{K} . In some cases, e.g. astronomical image restoration, an entropy can be calculated for the image function, which is then maximised by a regularisation functional [28].

Complementary to conventional physical and mathematical approaches, machine learning techniques are now emerging as powerful and computationally efficient tools for the study of glasses [29–34] and complex soft matter systems more generally [35]. As such, the recent explosion of interest in deep learning suggests a new route to extracting memory kernels from GLEs following the minimisation philosophy above. Deep Neural Networks (DNNs) have very attractive generalisation and expressivity properties [36–38], and so it is reasonable to ask whether a DNN could learn the mapping from the function y to the kernel K in Eq. 1. Such an approach has shown impressive results when applied to analytic problems with rapidly decaying memory kernels [39].

In this work we present a novel machine-learning based method for kernel extraction from GLE data. As a demonstration of effectiveness, we train and apply DNNs to the challenging problem of extracting memory kernels in glass-forming systems that have very long-lasting memory effects

and significant levels of noise. The networks are far more robust to noise in the input signal than traditional methods. Furthermore, we show that a network trained on data generated from analytic theory (hard-sphere MCT) generalises well to data from particle-based simulations of a different system. MCT provides an analytic, though approximate, memory kernel from which a training set can be generated, whereas with simulations we study the true dynamics, but with an unknown kernel. We have written a pipeline for users to train networks on their GLE system of choice, which is available at <https://github.com/mkerrwinter/KernelLearner>. Our network that has been trained on MCT data is available at https://zenodo.org/record/7603275#.Y_vAxS8wlpQ.

II. PROBLEM DEFINITION AND NUMERICAL SETUP

Our general method can be briefly summarised as follows. Starting from a set of memory kernels similar to those we wish to measure, training and testing sets are generated by solving the GLE using the same method as in [40], subjecting the solutions to many noise realisations, and using the (solution, kernel) pairs as input and output respectively. Multiple networks are trained over a range of hyperparameters, and an optimum network is selected which achieves the minimum test loss. Finally, a novel memory kernel can be measured from unseen input data, and validation can be performed by solving the GLE with this measured kernel to compare with the input. The “first guess” kernels could be derived from theory, generated to a low level of accuracy with existing kernel measurement methods, measured from a similar system, or simply be informed guesswork.

Our goal is to extract a memory kernel, $K(t)$, from the density autocorrelation function, $F(t)$, of a glassy system described by a GLE like Eq. 1. We use $F(t)$ curves generated by numerically solving MCT, as well as curves measured from particle-based simulations. The neural networks are trained on MCT data, and validation is performed on both unseen MCT data and simulation data. For comparison, we also extract the kernel by applying conventional (i.e. non-network) methods.

As the variable of interest, MCT typically employs the autocorrelation function

$$F(k, t) = \frac{1}{N} \langle \rho_{-\mathbf{k}}(0) \rho_{\mathbf{k}}(t) \rangle, \quad (3)$$

where $\rho_{\mathbf{k}} = \sum_j e^{i\mathbf{k} \cdot \mathbf{r}_j(t)}$ is the microscopic density in Fourier space, \mathbf{k} a wavevector, N the number of particles, and $\langle \cdot \rangle$ denotes an ensemble average. The overdamped MCT GLE has the form

$$\dot{F}(k, t) + \frac{D_0 k^2}{S(k)} F(k, t) + \int_0^t d\tau K_{\text{MCT}}(k, \tau) \dot{F}(k, t - \tau) = 0, \quad (4)$$

where $k = |\mathbf{k}|$ is the wavenumber, D_0 is the self-diffusion coefficient, $S(k) = F(k, 0)$ is called the static structure factor,

and K_{MCT} is the kernel. The MCT kernel is given by

$$K_{\text{MCT}}(k, t) = \frac{\rho D_0}{16\pi^3} \int d\mathbf{q} V_{\mathbf{q}, \mathbf{k}-\mathbf{q}}^2 F(q, t) F(|\mathbf{k}-\mathbf{q}|, t), \quad (5)$$

where the vertex term $V_{\mathbf{q}, \mathbf{k}-\mathbf{q}} = k^{-1}[\mathbf{k} \cdot \mathbf{q} c(q) + \mathbf{k} \cdot (\mathbf{k} - \mathbf{q}) c(|\mathbf{k} - \mathbf{q}|)]$, and $c(k) = \rho^{-1}[1 - 1/S(k)]$ (for more details see e.g. [3]). In general, $F(t)$ is a function of the wavenumber, and the MCT kernel couples different wavenumbers together. Equation 4 is subject to the initial condition $S(k) = F(k, 0)$.

To numerically solve the MCT equation we use the Percus-Yevick closure for a system of hard spheres [41, 42]. This is an analytic approximation for the static two-point correlation function $S(k)$ of a system of hard spheres at a given density. For simplicity, we test our method on the $F(k, t)$ behaviour at wavenumber $k = k^*$, corresponding to the main peak of $S(k)$. From here on we will omit the explicit k dependence and use $F(t) = F(k^*, t)$ for brevity.

The simulation data we use is from a system of particles interacting via the Weeks-Chandler-Andersen (WCA) potential [43]. Details of the simulations are given in Appendix B. Note that the type of particle in the simulation data (soft spheres) is different from the MCT data used to train the networks (hard spheres).

A. Dataset, network and training process

Both the training dataset and MCT testing dataset are produced in the same way. First, Eq. 4 is solved numerically at volume fractions $\phi \in \{0.45, 0.451, 0.452, \dots, 0.58\}$, that are symmetric about the MCT glass transition $\phi_g \approx 0.516$ [8], to produce a set of analytic curves denoted $F_A(t)$. Each curve is then subjected to 1000 different realisations of Gaussian noise like

$$F(t) = F_A(t) + \mu(\max(F_A) - \min(F_A))\xi(t), \quad (6)$$

where $\xi(t)$ is Gaussian noise with unit variance and zero mean, and $\langle \xi(t)\xi(t') \rangle = \delta(t - t')$. The parameter μ controls the strength of the noise. By adding noise to the training set the DNN learns the mapping from noisy dynamics to a clean memory kernel, and hence is able to handle real data measured from simulations or experiments. The dimension of the set of noisy curves, $\{F(t)\}$, is then reduced with Principle Component Analysis (PCA) where only the first 15 PCA components are retained [44]. The explained variance per component is shown in Fig. 1(b), which levels off at the 15th component. As well as the PCA components, we include the frequency term, $\Omega = \frac{D_0 k^2}{S(k)}$, and the value of the autocorrelation function at the final timepoint, $F(t_{\text{max}})$, in order to clearly distinguish between liquids ($F(t_{\text{max}}) = 0$) and glasses ($F(t_{\text{max}}) > 0$). The dimensionally reduced set of noisy curves, Ω , and $F(t_{\text{max}})$ form the input of the network, of dimension 17. The target is the K_{MCT} used to produce a given $F(t)$, discretised on a logarithmically spaced time grid of 100 points. Both the testing and the training set consist of $P = 65500$ such examples.

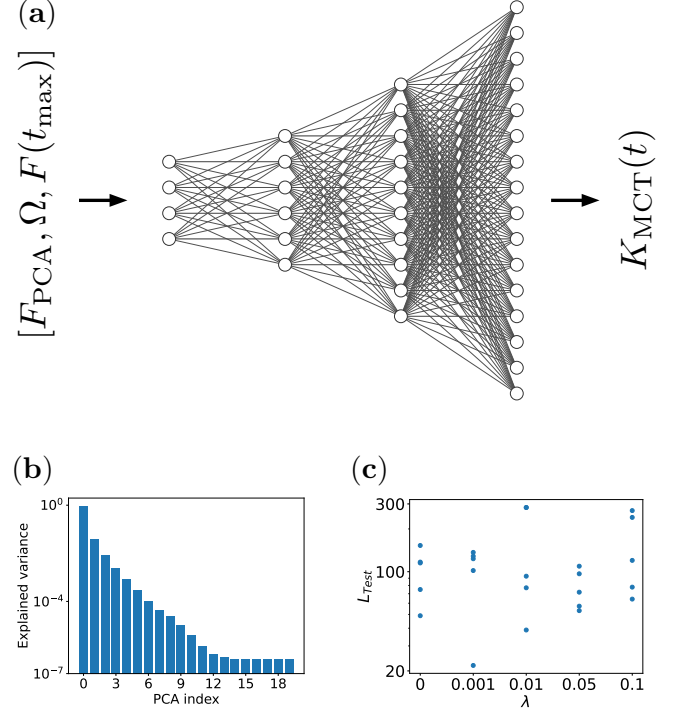


FIG. 1. (a) A schematic of the network structure. The input consists of the first 15 PCA components of a pairwise correlation function $F(t)$, the frequency term Ω , and the final correlation value $F(t_{\text{max}})$. The output is an approximation of the memory kernel used to generate $F(t)$ via Eq. 4 [45]. (b) The explained variance of consecutive PCA components of the training set, which display a kink between components 12 and 15. (c) Minimum test loss values for a subset of networks in the hyperparameter search. These networks have a width factor $\omega = 8$, and were trained with a batch size of 2500. The plot shows the variability between networks with different regularisation λ , and different initial conditions.

We use a fully connected feed-forward network with L layers, with input \mathbf{x} , and output given by

$$f_{\alpha}(\mathbf{x}, \Theta) = a_{\alpha}^{L+1}, \quad (7)$$

$$a_{\beta}^i = \sum_{\alpha} W_{\alpha\beta}^i \sigma(a_{\alpha}^{i-1}) - B_{\beta}^i, \quad 2 \leq i \leq L \quad (8)$$

$$a_{\beta}^1 = \sum_{\alpha} W_{\alpha\beta}^1 x_{\alpha} - B_{\beta}^1. \quad (9)$$

Greek letters index the matrices of weights between each layer, whereas Latin letters index the layers themselves, hence $W_{\alpha\beta}^i$ are the elements of the matrix of weights between layer $i - 1$ and i . The biases are given by B_{α}^i . The variable Θ is a vector containing all weights and biases. For the activation functions we choose the popular Rectified Linear Unit (ReLU), $\sigma(z) = \max(0, z)$. We use the dropout method to reduce overfitting [46], so that at each training step nodes are temporarily dropped from the network with probability $p = 0.5$. The network structure consists of $L = 6$ hidden layers that gradually increase in width. The hidden layer

widths are $[50\omega, 100\omega, 150\omega, 200\omega, 250\omega, 300\omega]$, where the width factor ω is an integer hyperparameter controlling the width of the network. The structure of the network, input, and output data is shown schematically in Fig. 1(a).

We use a weighted mean square error loss function between network output at neuron j , f_j , and true kernel $K(t_j)$, with L2 regularisation on the network parameters, Θ_k , to prevent overfitting [47],

$$L = \frac{1}{P} \sum_{i=1}^P \frac{1}{t_{\max}} \sum_{j=1}^{j_{\max}} \alpha_j (f_j - K(t_j))^2 + \lambda \sum_{k=1}^M \Theta_k^2, \quad (10)$$

where the first sum is over examples in the training set, and the second is over the time points t_j at which K is discretised. The weights increase linearly with the time grid, $\alpha_j = j/j_{\max}$, so that long-time behaviour is given more importance. This is because the kernel at long times affects the dynamics to a greater extent than at short times. The parameter λ controls the strength of L2 regularisation over the M network parameters. Training is performed using the Adam method, a popular stochastic gradient descent algorithm [48].

B. Non-network methods

For comparison with the above network-based method, we also implement two traditional kernel extraction methods. The first applies an inverse Laplace transform to Eq. 2. We use the De Hoog algorithm to evaluate \mathcal{L}^{-1} using a Fourier series with accelerated convergence [49, 50]. This method outperformed other common inversion algorithms (Talbot [51] and Stehfest [52]) on our data. To mitigate the effect of noise we first smooth the $F(t)$ curves with a Savitzky-Golay filter [53] before applying the De Hoog inverter. The second method is to construct and solve a Volterra integral equation for K , the details of which are given in Appendix E.

III. RESULTS

A. Hyperparameter search

We first search for optimum network hyperparameters. As there are a large number of hyperparameters that can be optimised a full grid search is unfeasible. Instead, we choose the L2 regularisation strength λ , the batch size of the Adam method, and the width factor ω as the most important hyperparameters, and perform a search over reasonable intervals for each. This process is shown for λ in Fig. 1(c), where multiple initial conditions have been included for each λ . As well as demonstrating the effect of λ on the test loss, this figure illustrates the significant randomness introduced by using different initial conditions for Θ , and hence the importance of training multiple networks with different initial conditions. We select the network with the lowest test loss across the whole hyperparameter search.

B. Performance on MCT Percus-Yevick hard spheres

We apply our optimum network to the task of extracting memory kernels from unseen $F(t)$ curves generated by hard sphere MCT and subjected to noise according to Eq. 6. For comparison, we use the De Hoog algorithm to extract the kernel by means of Eq. 2 applied to noisy $F(t)$ curves. It is reasonable to ask whether a simple smoothing procedure to mitigate the effect of noise would be sufficient to achieve reasonable performance without resorting to deep learning. To investigate this, we also use the De Hoog algorithm on $F(t)$ curves that have been smoothed by a Savitzky-Golay filter.

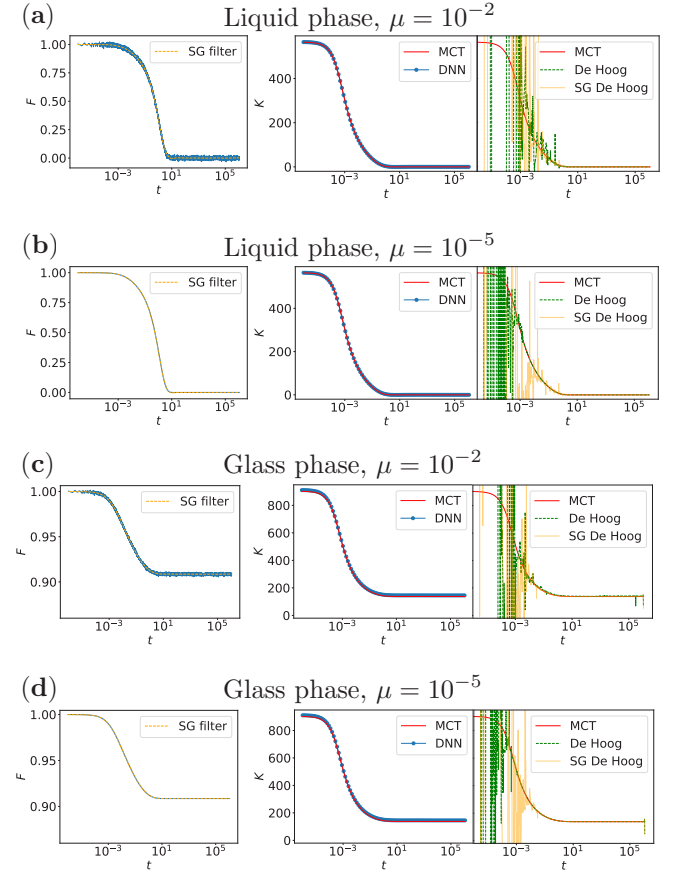


FIG. 2. Examples of kernel extraction from a density autocorrelation function using a trained network and the De Hoog algorithm. (a) The liquid phase of Percus-Yevick Hard Sphere MCT with volume fraction $\phi = 0.475$. The left-hand panel shows the noisy $F(t)$ curve, with $\mu = 10^{-2}$ as defined in Eq. 6, as well as the smoothed curve produced by the Savitzky-Golay filter. The middle panel contains the memory kernel as measured by a network and the true MCT kernel. The right-hand panel contains the kernel measured by the De Hoog algorithm from the smoothed $F(t)$ ('SG De Hoog'), the kernel measured from the raw noisy curve ('De Hoog'), and the true MCT kernel. (b) The same curves measured from $F(t)$ at $\phi = 0.475$ with $\mu = 10^{-5}$. (c) and (d) are the same measurements again but in the glass phase with $\phi = 0.52$.

The left-hand panels of Fig. 2 show both the noisy and

smoothed $F(t)$. The two right-hand panels show the kernel measured by our neural network, Laplace inversion of Eq. 2, and Laplace inversion of Eq. 2 using the smoothed $F(t)$. We measure kernels in both the liquid (volume fraction $\phi = 0.475$) and glass ($\phi = 0.52$) regimes, subjected to both high ($\mu = 10^{-2}$) and low ($\mu = 10^{-5}$) levels of noise. In all cases the network reproduces the true MCT kernel from $F(t)$ to a very high degree of accuracy. In contrast, Laplace inversion fails to produce an accurate (or indeed even vaguely reasonable) kernel across all times. Although the smoothing process on $F(t)$ in the left-hand panel of Fig. 2(a) and (c) looks very effective by eye, it does not significantly improve the accuracy of the measured kernel. As can be seen in the low noise plots, Fig. 2(b) and (d), the noise on $F(t)$ must be reduced to the point where it is no longer visible by eye before conventional Laplace inversion can measure a reasonable kernel over multiple decades. Even then, this approach fails at short times. Interestingly, when noise is this low the smoothing process actually decreases performance.

In Appendix C we demonstrate that the DNN hugely outperforms De Hoog Laplace inversion once again, this time very close to the glass transition point. This is a particularly challenging region of parameter space as $F(t)$ becomes very sensitive to small changes in the initial conditions. Fig. 5 in Appendix D shows how the network extrapolates well to regions of phase space not included in the training set. The ability to generalise is crucial for the usefulness of the DNN method. The caveat to this extrapolation is that deep in the glass phase, at volume fractions higher than those in the training set, the dynamics become only weakly dependent on the kernel and the performance of the network decreases.

The results in Fig. 2 demonstrate the extreme susceptibility of Laplace inversion to noise, as well as the huge improvement achieved by deep learning. Furthermore, as shown in Appendices C and D, our network method is highly effective in difficult regions of parameter space, and in regions not included in the training set. Finally, the trained DNN is hundreds of times faster than the De Hoog algorithm. Our deep learning method comprehensively outperforms conventional Laplace inversion for measuring the memory kernel of hard sphere MCT.

C. Performance on simulated soft spheres

To test the limits of the network's performance, we apply it to data from a different system than the one it was trained on. We run Brownian dynamics simulations of WCA monodisperse spheres (see Appendix B), and measure $F(t)$ both from single trajectories, and an ensemble average of several hundred trajectories. We measure kernels by two methods, namely from our neural network, and by constructing an implicit Volterra integral equation for K (see Appendix E). The neural network has not been retrained, i.e. it has only seen the MCT hard sphere training set of the previous section. This is in order to study the ability of the network to generalise to an unseen system. For validation, we solve Eq. 4 using the kernels measured by the network or Volterra method in place of K_{MCT} , resulting in a new $F(t)$ curve which we can compare

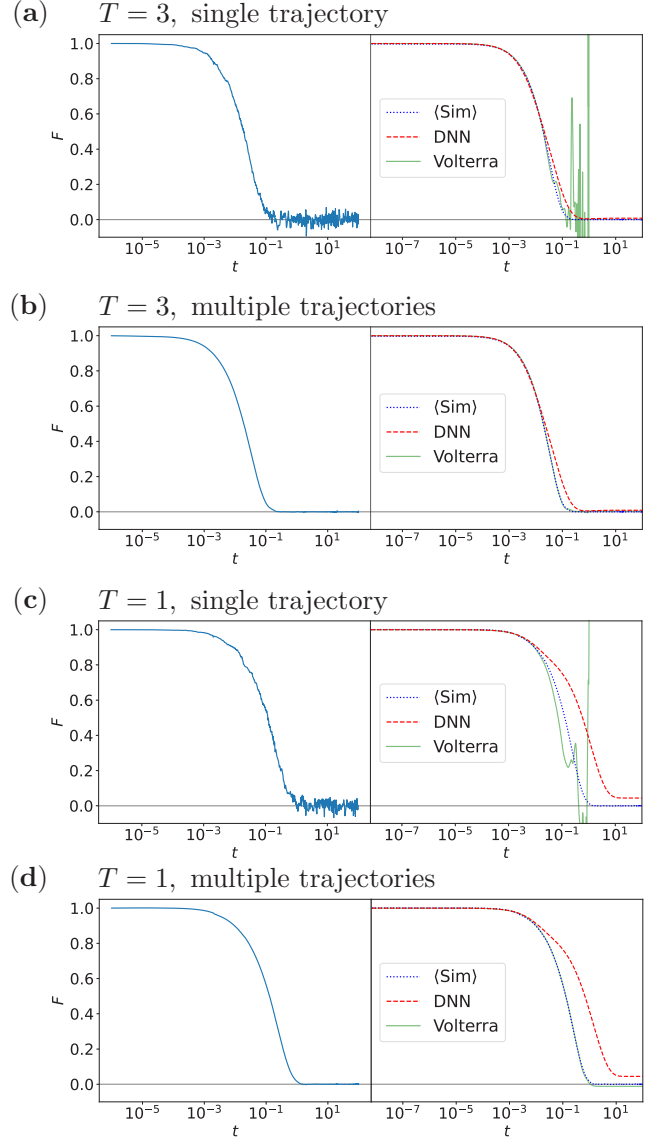


FIG. 3. Reproducing $F(t)$ from WCA simulations. In the left-hand panels of (a) and (c), $F(t)$ is calculated from a single simulation trajectory and hence exhibits significant levels of noise. In the left-hand panels of (b) and (d) and in the right-hand panels clean $F(t)$ curves are produced by averaging over many trajectories ($\langle \text{Sim} \rangle$). Kernels are measured from $F(t)$ with the network ('DNN') and Volterra ('Volterra') methods, which are then used to solve Eq. 4. The resulting $F(t)$ curves are plotted in the right-hand panels. A perfect kernel measurement would result in exactly the same curve as $\langle \text{Sim} \rangle$. In the low-noise plots the Volterra line is almost indistinguishable from the data. Temperatures are in Lennard-Jones units, defined in Appendix B.

with $F(t)$ from the simulations.

In Fig. 3(a) the noisy $F(t)$ of a single simulation trajectory (left-hand panel) is used as input. The network is able to reproduce dynamics that are very close to the true dynamics of the system calculated by averaging many trajectories (right-hand panel). In contrast, the Volterra method begins to

oscillate wildly and soon diverges. The same measurements are repeated at a lower temperature (but still in the normal liquid regime) in Fig. 3(c). Similar to the hard-sphere case, the DNN method hugely outperforms traditional methods in the presence of noise. In Fig. 3(b) and (d) the input data is the ensemble-averaged $F(t)$. The right-hand panels compare the dynamics using the network kernel, and the Volterra kernel, to the true dynamics from the left-hand panel. In this low-noise context the Volterra method performs very well. At high T the network is able to produce dynamics that are very similar to the ground truth, whereas at low T the network is less accurate, but not catastrophically so. Importantly, the network-predicted dynamics exhibit an incorrect non-zero plateau at long times. The long-time behaviour of $F(t)$ is very sensitive to the long-time behaviour of K , hence small non-zero values in the tail of K (a likely outcome of any minimisation routine) can result in a non-zero tail in $F(t)$.

It is important to recall that the DNN has not been retrained on the soft sphere simulations. The input data in Fig. 3 differs from the training set in how it was generated (simulation vs theory), the nature of the noise on $F(t)$, and in the system itself (WCA vs hard spheres). Despite these multiple differences, our results demonstrate how well our DNN method generalises to new systems. Furthermore, the network can reproduce ensemble-averaged dynamics from noisy data, unlike conventional methods, allowing a clean measurement to be made from a single simulation trajectory.

IV. CONCLUSION

In this work we develop a novel deep learning method for measuring the memory kernel of GLEs. Our method is generally applicable to any GLE system where a training set can be constructed. We demonstrate its effectiveness on MCT hard sphere data, and show that the DNN measures highly accurate kernels on unseen inputs, with particular robustness to noise. This is in stark contrast with existing Laplace inversion methods that are highly sensitive to noise. Furthermore, the DNN method generalises well to a system different from that used for training.

Our DNN method has several attractive features. It is computationally efficient as the time to make predictions with a trained network is negligible. It also makes no distinction between short or long memory effects. This is in contrast to existing iterative techniques where errors accumulate over long times, posing a particular problem with long-lived glassy kernels. The ability of the DNN to map noisy single trajectory inputs to clean, ensemble averaged outputs is particularly powerful, allowing it to be used in situations where it is difficult to measure multiple trajectories for averaging, e.g. costly simulations or experiments.

As is the case with any machine learning technique, the network performs less well when presented with data that is dissimilar to that used during training, as seen with the low-temperature WCA data with low noise in Fig. 3(d). However, this shortcoming can be addressed by including more diverse examples in the training set. As such, we

present our code as a pipeline for training networks on data of the user's choosing, as well as our own trained network for the case of hard spheres. Giving users the tools to train networks on their specific problem will result in significantly smaller, yet better performing, networks than attempting to train a general-purpose GLE kernel extractor. The success with which neural networks can learn the highly non-trivial mapping between $F(t)$ and K suggests that deep learning techniques should be considered for a diverse range of inverse problems where a training set can be generated by solving the simpler forward problem.

V. ACKNOWLEDGEMENTS

This work was financially supported by the Dutch Research Council (NWO) through a START-UP grant (MKW, VED, and LMCJ) and Vidi grant (IP and LMCJ).

Appendix A: Hyperparameter search

A hyperparameter search was performed over the L2 regularisation parameter, λ , the batch size, B , and width factor, ω . For each combination of parameters, 5 networks with different initial conditions were trained. The initial condition was set by drawing weights and biases from a random uniform distribution $U(-\sqrt{k}, \sqrt{k})$, where $1/k$ is the number of input features to the layer. The hyperparameter values in the search were

- λ : 0.1, 0.05, 0.01, 0.001, 0
- B : 300, 2500, 10000
- ω : 2, 4, 8,

resulting in a total of $5 \times 3 \times 3 \times 5 = 225$ networks.

Appendix B: Simulation details

Simulations were performed of a set of $N = 2000$ Brownian particles in 3D, with periodic boundary conditions and a number density $\rho = 0.95$. The position of particle i , \mathbf{r}_i , obeys the overdamped Langevin equation,

$$\dot{\mathbf{r}}_i = \zeta^{-1} \mathbf{F}_i + \boldsymbol{\xi}_i(t), \quad (\text{B1})$$

where $\zeta = 1$ is a friction coefficient, \mathbf{F}_i is a force acting on particle i due to the inter-particle potential, and $\boldsymbol{\xi}_i$ is a random noise term obeying $\langle \boldsymbol{\xi}_i(t) \rangle = \mathbf{0}$, and $\langle \boldsymbol{\xi}_i(t) \cdot \boldsymbol{\xi}_j(t') \rangle = 6D_0 \delta_{ij} \delta(t - t')$, where $D_0 = k_B T / \zeta$ is the diffusion constant, k_B the Boltzmann constant, and T the temperature. The interaction force comes from the Weeks-Chandler-Andersen potential,

$$U(r) = 4\epsilon \left[\left(\frac{\sigma}{r} \right)^{12} - \left(\frac{\sigma}{r} \right)^6 \right] + \epsilon, \quad (\text{B2})$$

where r is the inter-particle distance. We use Lennard-Jones units such that $\sigma = 1$ is the particle diameter, and $\epsilon = 1$ a parameter determining the strength of the interaction. A dimensionless temperature can be defined as $T^* = k_B T / \epsilon$. $U(r)$ is truncated such that the potential is purely repulsive. The simulations were performed with the LAMMPS molecular dynamics software [54] with timestep $\Delta t = 10^{-5}$. The system is left to evolve for 10^7 timesteps to equilibrate, then measurements are taken over a further 10^7 timesteps.

Appendix C: Performance near the glass transition

A particularly challenging task is to measure an accurate memory kernel very close to the glass transition. At this point the dynamics of $F(t)$ are strongly dependent on small changes in K . Nevertheless, our DNN is capable of measuring K to a high degree of accuracy as shown in Fig. 4, once again hugely outperforming conventional Laplace inversion algorithms.

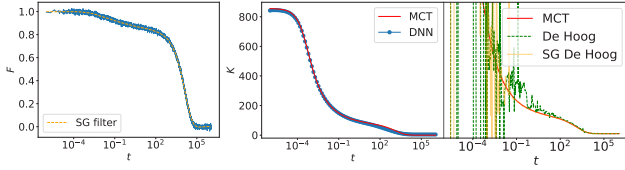


FIG. 4. Kernels extracted from $F(t)$ (left-hand panel) by DNN (middle panel) and by the De Hoog algorithm applied to both noisy and smoothed data (right-hand panel). Here, the volume fraction $\phi = 0.515$ is very close to the MCT glass transition volume fraction which lies between $0.515 < \phi_g < 0.516$.

Appendix D: Exploring unseen phase space

The network is trained on a set of $F(t)$ curves generated at volume fractions $\phi \in \{0.45, 0.451, 0.452, \dots, 0.58\}$, and subjected to multiple noise realisations. How does the network perform on volume fractions that are not in the training set? This question is addressed in Fig. 5. Fig. 5(a) shows the performance of the network at a volume fraction below the range of the training set. The left-hand panel is the input noisy $F(t)$, and the right-hand panel shows the measured K , which agrees with the true MCT kernel to a high degree of accuracy, with a small discrepancy at very short times. Fig. 5(b) is at a volume fraction that is not in the training set, but is within the range of training ϕ values. In this case the network measures a highly accurate kernel, as it does at ϕ values in the training set. Fig. 5(c) and (d) are at volume fractions above the upper end of the training set. Here the measured kernel is inaccurate. The reason for this can be seen in the $F(t)$ curves in the left-hand panels. At $\phi = 0.59$ and $\phi = 0.62$ we are deep in the glass phase, and the system decorrelates very little (i.e. the asymptote of $F(t)$ at long times is greater than 0.99 in both cases). As such, the dynamics become less and less sensitive to the exact form of the memory kernel. These plots demonstrate

that the network can generalise well to regions of phase space beyond the training set, however care must be taken. For some parameter values (e.g. ϕ deep in the glass phase) the network is insufficiently sensitive to the weak relationship between K and $F(t)$.

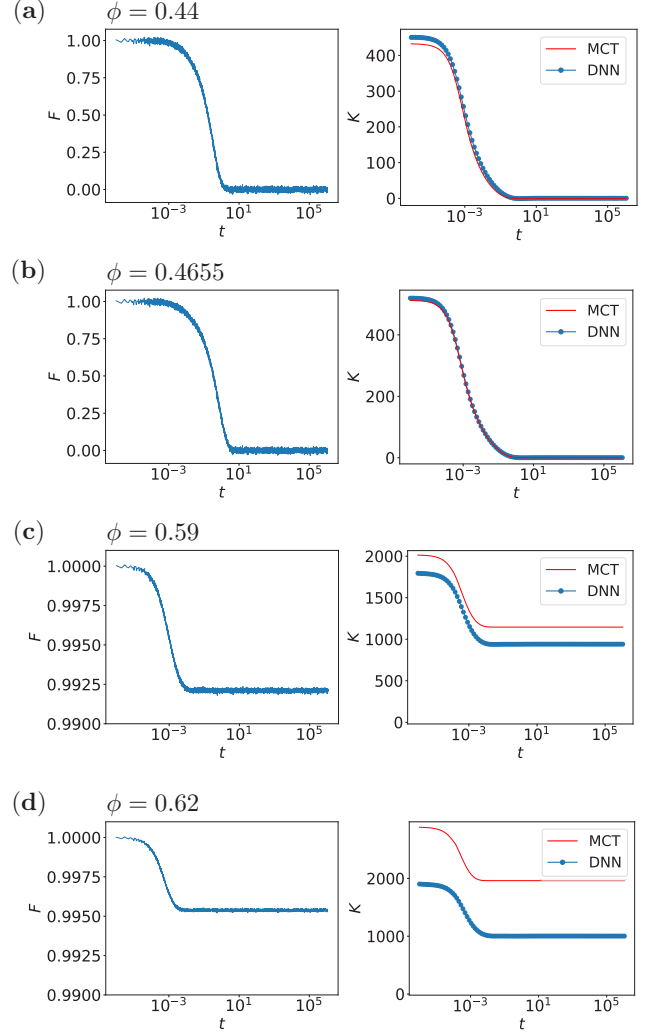


FIG. 5. $F(t)$ curves and the corresponding kernels, ground truth given by MCT and approximated by the network, at volume fractions not in the training set. (a) Below the lowest ϕ in the training set. (b) Between values in the training set. (c) and (d) Above the highest value in the training set.

Appendix E: Volterra Method

Our goal is to find an expression for the irreducible memory kernel $K(k, t) = \frac{1}{Nk^2 D_0} \langle R_{\mathbf{k}}^* e^{\Omega^\dagger \mathcal{Q}' \mathcal{Q} t} R_{\mathbf{k}} \rangle$. Here, $R_{\mathbf{k}} = \mathcal{Q} \Omega^\dagger \rho_{\mathbf{k}}$ is the fluctuating force, Ω^\dagger is the conjugate of the Smoluchowski operator, and $\mathcal{Q} = 1 - \mathcal{P}$ is the projector on the space orthogonal to that spanned by the density modes,

given by $\mathcal{P} = \rho_{\mathbf{k}} \langle \rho_{\mathbf{k}}^* \rho_{\mathbf{k}} \rangle^{-1} \langle \rho_{\mathbf{k}}^* \cdot$. Additionally, we have defined a second projection $\mathcal{P}' = \rho_{\mathbf{k}} \langle \rho_{\mathbf{k}}^* \Omega^\dagger \rho_{\mathbf{k}} \rangle^{-1} \langle \rho_{\mathbf{k}}^* \Omega^\dagger$, and its complement $\mathcal{Q}' = 1 - \mathcal{P}'$ (for more details see [55] and [56]).

Since the evolution operator $e^{\Omega^\dagger \mathcal{Q}' \mathcal{Q} t}$ is hard to deal with, we apply the Dyson decomposition identity,

$$e^{\Omega^\dagger \mathcal{Q}' \mathcal{Q} t} = e^{\Omega^\dagger t} - \int_0^t d\tau e^{\Omega^\dagger \mathcal{Q}' \mathcal{Q} (t-\tau)} \Omega^\dagger (1 - \mathcal{Q}' \mathcal{Q}) e^{\Omega^\dagger \tau}, \quad (\text{E1})$$

which yields a Volterra equation for the memory kernel

$$K(k, t) = K_{\Omega^\dagger}(k, t) + \int_0^t d\tau K(k, t - \tau) W(k, \tau). \quad (\text{E2})$$

Here we have introduced the function

$$K_{\Omega^\dagger}(k, t) = (Nk^2 D)^{-1} \left\langle R_{\mathbf{k}}^* e^{\Omega^\dagger t} R_{\mathbf{k}} \right\rangle, \quad (\text{E3})$$

and the correlation

$$W(k, t) = (Nk^2 D)^{-1} \left\langle \rho_{\mathbf{k}}^* \Omega^\dagger e^{\Omega^\dagger t} R_{\mathbf{k}} \right\rangle, \quad (\text{E4})$$

which both evolve with standard Brownian dynamics.

In order to solve the integral equation (E2), we first compute $K_{\Omega^\dagger}(k, t)$ and $W(k, t)$ at $k = 7.0$ from the simulation trajectories. This we do by evaluating their definitions (E3) and (E4), averaging over 50 independently initialised simulation trajectories, a small number of time origins, and all allowed wave vectors in the range $k \in (7.0 \pm 0.1)$. We refer to averaging over both independent simulation trajectories and time origins as an ensemble average. For Fig. 3(a) and (c), we omit the ensemble and time-origin average, in order to introduce more noise.

Either the single trajectory or ensemble-averaged $K_{\Omega^\dagger}(k, t)$ and $W(k, t)$ are inserted in a discretised version of integral equation (E2). The memory kernel is subsequently found by solving the resulting system of equations [57].

-
- [1] C. L. E. Franzke, T. J. O’Kane, J. Berner, P. D. Williams, and V. Lucarini, *Wiley Interdisciplinary Reviews: Climate Change* **6** (2015), 10.1002/wcc.318, arXiv:1409.0423.
 - [2] E. Herrera-Delgado, R. Perez-Carrasco, J. Briscoe, and P. Sollich, *PLoS Computational Biology* **14** (2018), 10.1371/journal.pcbi.1006003, arXiv:1708.09312.
 - [3] L. M. C. Janssen, *Frontiers in Physics* **6** (2018), 10.3389/fphy.2018.00097, arXiv:1806.01369.
 - [4] P. G. Debenedetti and F. H. Stillinger, *Nature* **410** (2001).
 - [5] D. R. Reichman and P. Charbonneau, *Journal of Statistical Mechanics: Theory and Experiment*, P05013 (2005).
 - [6] R. Zwanzig, *Physical Review* **124** (1961), 10.1103/PhysRev.124.983.
 - [7] H. Mori, *Progress of Theoretical Physics* **33** (1965).
 - [8] U. Bengtzelius, W. Götze, and A. Sjölander, *Journal of Physics C: Solid State Physics* **17** (1984), 10.1080/01411599408200364.
 - [9] E. Leutheusser, *Physical Review A* **29** (1984), 10.1103/PhysRevA.29.2765.
 - [10] S. P. Das, *Reviews of Modern Physics* **76** (2004), 10.1103/RevModPhys.76.785.
 - [11] W. Götze, *Complex Dynamics of Glass-Forming Liquids: A Mode-Coupling Theory* (Oxford University Press, 2008).
 - [12] G. Szamel, *Physical Review Letters* **90**, 228301 (2003), arXiv:0305626.
 - [13] S. P. Das and G. F. Mazenko, *Physical Review A* **34**, 2265 (1986).
 - [14] W. Götze and L. Sjögren, *Zeitschrift für Physik B Condensed Matter* **65**, 415 (1987).
 - [15] C. Luo and L. M. C. Janssen, *Journal of Chemical Physics* **153** (2020), 10.1063/5.0026969, arXiv:1909.00428.
 - [16] L. M. C. Janssen and D. R. Reichman, *Physical Review Letters* **115**, 205701 (2015), arXiv:1507.01947.
 - [17] J. G. McWhirter and E. R. Pike, *Journal of Physics A: Mathematical and General* **11** (1978), 10.1088/0305-4470/11/9/007.
 - [18] I. J. D. Craig and A. M. Thompson, *Computers in Physics* **8** (1994), 10.1063/1.4823347.
 - [19] C. L. Epstein and J. Schotland, *SIAM Review* **50** (2008), 10.1137/060657273.
 - [20] M. Baity-Jesi and D. R. Reichman, *Journal of Chemical Physics* **151**, 084503 (2019), arXiv:1906.05818.
 - [21] H. Vroylandt and P. Monmarché, *Journal of Chemical Physics* **156**, 244105 (2022), arXiv:2201.02457.
 - [22] Y. Han, J. Jin, and G. A. Voth, *Journal of Chemical Physics* **154**, 084122 (2021).
 - [23] S. Cao, A. Montoya-Castillo, W. Wang, T. E. Markland, and X. Huang, *Journal of Chemical Physics* **153**, 014105 (2020).
 - [24] G. Jung, M. Hanke, and F. Schmid, *Journal of Chemical Theory and Computation* **13**, 2481 (2017), arXiv:1709.07805.
 - [25] B. Kowalik, J. O. Daldrop, J. Kappler, J. C. F. Schulz, A. Schlaich, and R. R. Netz, *Physical Review E* **100**, 012126 (2019).
 - [26] M. Berkowitz, J. D. Morgan, D. J. Kouri, and J. A. McCammon, *The Journal of Chemical Physics* **75**, 2462 (1981).
 - [27] Q. Shi and E. Geva, *Journal of Chemical Physics* **120**, 10647 (2004).
 - [28] R. Narayan and R. Nityananda, *Annual Review of Astronomy and Astrophysics* **24** (1986), 10.1146/annurev.astro.24.1.127.
 - [29] S. S. Schoenholz, E. D. Cubuk, D. M. Sussman, E. Kaxiras, and A. J. Liu, *Nature Physics* **12** (2016), 10.1038/nphys3644, arXiv:1506.07772.
 - [30] I. Tah, S. A. Ridout, and A. J. Liu, *The Journal of Chemical Physics* **157**, 124501 (2022), arXiv:2205.07187.
 - [31] R. M. Alkemade, E. Boattini, L. Filion, and F. Smallenburg, *Journal of Chemical Physics* **156**, 204503 (2022).
 - [32] D. Coslovich, R. L. Jack, and J. Paret, *Journal of Chemical Physics* **157**, 204503 (2022), arXiv:2211.01904.
 - [33] J. Paret, R. L. Jack, and D. Coslovich, *Journal of Chemical Physics* **152**, 144502 (2020), arXiv:2002.02726.
 - [34] V. Bapst, T. Keck, A. Grabska-Barwińska, C. Donner, E. D.

- Cubuk, S. S. Schoenholz, A. Obika, A. W. Nelson, T. Back, D. Hassabis, and P. Kohli, *Nature Physics* **16**, 448 (2020).
- [35] G. Campos-Villalobos, E. Boattini, L. Filion, and M. Dijkstra, *Journal of Chemical Physics* **155**, 174902 (2021).
- [36] S. L. Smith, E. Elsen, and S. De, *Proceedings of the 37th International Conference on Machine Learning* (2020), arXiv:2006.15081.
- [37] D. S. Park, J. Sohl-Dickstein, Q. V. Le, and S. L. Smith, *36th International Conference on Machine Learning, ICML 2019*, 8857 (2019), arXiv:1905.03776.
- [38] K. Hornik, M. Stinchcombe, and H. White, *Neural Networks* **2** (1989), 10.1016/0893-6080(89)90020-8.
- [39] R. Fournier, L. Wang, O. V. Yazyev, and Q. S. Wu, *Physical Review Letters* **124**, 056401 (2020), arXiv:1810.00913.
- [40] V. E. Debets, C. Luo, S. Ciarella, and L. M. C. Janssen, *Physical Review E* **104**, 065302 (2021), arXiv:2108.06829.
- [41] J. K. Percus and G. J. Yeck, *Physical Review* **110**, 1 (1958).
- [42] M. S. Wertheim, *Physical Review Letters* **10**, 321 (1963).
- [43] J. D. Weeks, D. Chandler, and H. C. Andersen, *The Journal of Chemical Physics* **54**, 5237 (1971).
- [44] I. T. Jolliffe, *Principal Component Analysis*, 2nd ed. (Springer New York, 2002).
- [45] A. Lenail, “alexlenail.me/NN-SVG/,” (2023).
- [46] N. Srivastava, G. Hinton, A. Krizhevsky, I. Sutskever, and R. Salakhutdinov, *Journal of Machine Learning Research* **15** (2014).
- [47] X. Ying, *Journal of Physics: Conference Series* **1168** (2019).
- [48] D. P. Kingma and J. L. Ba, *3rd International Conference on Learning Representations* (2015), arXiv:1412.6980.
- [49] F. R. de Hoog, J. H. Knight, and A. N. Stokes, *SIAM Journal on Scientific and Statistical Computing* **3**, 357 (1982).
- [50] K. L. Kuhlman, *Numerical Algorithms* **63**, 339 (2013), arXiv:1204.4754.
- [51] A. Talbot, *IMA Journal of Numerical Analysis* **23**, 97 (1979).
- [52] H. Stehfest, *Communications of the ACM* **13**, 47 (1970).
- [53] A. Savitzky and M. J. E. Golay, *Analytical Chemistry* **36**, 1627 (1964).
- [54] A. P. Thompson, H. M. Aktulga, R. Berger, D. S. Bolintineanu, W. M. Brown, P. S. Crozier, P. J. in ’t Veld, A. Kohlmeyer, S. G. Moore, T. D. Nguyen, R. Shan, M. J. Stevens, J. Tranchida, C. Trott, and S. J. Plimpton, *Computer Physics Communications* **271**, 108171 (2022).
- [55] G. Nägele, *Physics Report* **272** (1996), 10.1016/0370-1573(95)00078-X.
- [56] G. Nägele, J. Bergenholtz, and J. K. Dhont, *Journal of Chemical Physics* **110**, 7037 (1999).
- [57] I. Pihlajamaa, V. E. Debets, C. C. L. Laudicina, and L. M. C. Janssen, *Soon to be published*.